Optical properties of TiO₂@C nanocomposites: Synthesized by green synthesis technique

Srikanta Karmakar[1], Subrata Biswas[1], Pathik Kumbhakar[1*], Tapan Ganguly[2]

[1]*Nanoscience Laboratory, Dept. of Physics, National Institute of Technology, Durgapur, 713209, West Bengal, India*
[2]*School of Laser Science and Engg., Jadavpur University, Jadavpur, Kolkata, 700032, West Bengal, India*

*Corresponding author, Tel: (+91) 0343-2754777; E-mail: nitdgpkumbhakar@yahoo.com;
pathik.kumbhakar@phy.nitdgp.ac.in

Abstract

In this work, we have reported an eco-friendly and cost-effective technique of synthesis of TiO₂@Carbon nanocomposites (TCNs) material by a facile solvothermal treatment of banana (*Musa balbisiana*) bract extract. Yellow green photoluminescence (PL) feature and efficient catalytic activities of green synthesized TCNs have been demonstrated. X-ray diffraction (XRD) data has revealed the simultaneous presence of rutile and anatase phases of TiO₂ in the synthesized TCNs. The presence of amorphous carbon and TiO₂ is also confirmed by Raman spectroscopy. The light emission characteristics of TCNs are studied by PL emission spectroscopy which has confirmed the presence of defect levels caused by oxygen vacancies and surface hydroxyl groups localized within the band-gap.The photo-catalytic performance of the synthesized material has been systematically evaluated by observing the degradation of Methylene Blue (MB) dye under the incidence of ultraviolet-visible (UV-Vis)/visible light irradiation and manifested a superior UV-Vis light photo-catalytic activity far over the commercial TiO₂ powder (CTP) under the same experimental conditions. A relatively higher electrochemical performance and 52 times larger cathodic current density is obtained in TCNs in compared to that of CTP. TCNs exhibit extremely high hydrogen evolution reaction catalytic activity with very small onset over potential. Copyright © 2017 VBRI Press.

Keywords: Green synthesis, TiO₂-Carbon nanocomposite, optical properties, photoluminescence emission.

Introduction

Researchers have put enormous efforts in the recent past to develop semiconductor nanoparticles based effective photo-catalyst for removal of the organic pollutants from water. Semiconductor nanomaterials, especially metal and metal oxide, like ZnO, ZnS, and TiO₂ have been widely used for remediation of environmental pollutants and in waste water treatment due to their high photo-catalytic efficiency and easy method of synthesis. Amongst all other metal oxide nanoparticles, TiO₂ has been extensively studied for its potential applications in photo-catalysis due to its low cost, nontoxic, high redox ability and stability. In order to make TiO₂ as visible-light-active photo-catalyst usually transition metal ions such as V, Cr, Mn, Fe, Ag, Co, Ni and C are doped. Doping of carbon into TiO₂ or making TiO₂-carbon nanocomposite extends the light absorption into the visible region. The preparation of TiO₂-carbon nanocomposites has been investigated by using various methods such as, hydrothermal **[1]**, solvothermal **[2]**, sol–gel **[3, 4]** sonochemical **[5]**, sputtering **[6]** etc. But these methods are costly, toxic, required high pressure and high energy, difficult separation technique and potentially hazardous. Recently, Nasrollahzadeh *et al*. **[7]** have reported eco-friendly green synthesis techniques to synthesize Pd/TiO₂

nanoparticles from *Myrtus communis* L. leaf extract**.** Shabani *et al*. **[8]** have been successfully synthesized TiO₂ nanoparticles in the presence of pomegranate juice. Hudlikar *et al*. **[9]** have successfully synthesized TiO₂ nanoparticles using plant extract of Jatropha curcas L. Latex. These green synthesis techniques are low cost, fast and also the formation of crystalline nanoparticles with a variety of shapes and sizes with high yield are possible. However, in all above earlier reports researchers have used different salts as precursors for synthesizing TiO₂ nanoparticles or nanostructures. Among the various biosynthetic approaches, the use of plant extracts has several advantages, such as easy availability of the precursor raw material, nontoxicity, easy to handle and low cost. Hence development of a reliable biosynthetic, an environment eco-friendly approach is essentially demanding having interesting properties, such as use of eco-friendly products, economic viability in the long run, and biocompatibility.

In the process of biosynthesis of nanoparticles, being a kind of bottom up approach, the main reaction is reduction/oxidation. Recently, Wang *et al.* **[10]** have demonstrated synthesis of TiO₂/carbon dots nanocomposite from the hydrothermal treatment of natural vegetables, including red pepper, guava, peas and spinach. Out of various methods available for the

synthesis of TiO_2 and carbon nanocomposites, the solvothermal method has been widely used as a simplistic and effective low temperature method to synthesize carbon@TiO_2 nanostructures [2]. However, the biosynthetic route for the synthesis of TCNs particularly with banana bract has not been reported, yet. Previously TiO_2 and TiO_2/activated carbon composite have been synthesized from Ilmenite ore and they have found the existence of mixed phase TiO_2 [11, 12]. Foo *et al*. [12] have extracted titanium dioxide from mineral Ilmenite by digestion of Ilmenite with strong sulphuric acids subsequently by hydrolysis and precipitation.

Previously, Lin *et al*. [13] have synthesized C-TiO_2 nanocomposites by a simple hydrothermal process and they have showed up to 70% degradation of MB dye within 2 h. Liu *et al*. [14] have reported that the carbon-titania nanocomposites exhibit excellent photocatalytic activity in aqueous suspensions. Yu *et al*. [15] have suggested that the mesoporous TiO_2@C nanocomposites will have the advantage of coupling the photoactivity of TiO_2 with the adsorptive capacity of carbon. In TiO_2@C nanocomposite carbon phase prevents the growth of nanocrystals and improves the thermal stability of the system. Also, Hurum *et al*. [16] have shown that the surface-phase junction between the rutile and anatase nanoparticles in mixed phase TiO_2 may cause greater photocatalytic activity.

However, in this work we have reported, for the first time, *in situ* solvothermal technique to synthesize TiO_2@C nanocomposites by using an eco-friendly technique and by using easily available banana (*Musa balbisiana*) bract extract without using any reducing material or external chemical agent and relatively at a low reaction temperature of 140°C. The simultaneous presences of rutile and anatase phases of TiO_2 have been identified successfully by XRD and Raman spectroscopy data analyses. The presence of amorphous carbon is identified by Raman spectroscopy, UV-Vis absorbance and photoluminescence (PL) emission spectral data analyses. Ilmenite is present in the soil of the district of Bankura and Purulia of West Bengal, India (according to database of Directorate of Mines & Minerals, Government of West Bengal-http://www.dmm.gov.in/htmls/mineral inventory. html) from where we have collected banana bract. This has perhaps led to the formation of TiO_2@C nanocomposite after solvothermal treatment of banana bract extract prepared in methanol medium. The synthesized TCNs showed efficient PL emission covering the entire visible range of the electromagnetic spectrum with the calculated Commission Internationale de I'Eclairage 1931 (CIE) chromaticity coordinate of (0.22, 0.27), which is almost same as that of yellowish-green light. Photo-catalytic degradation experiments of MB dye has been conducted under the incidence of both UV-Vis and visible lights. MB dye degradation efficiency as high as 84% has been achieved within 100 min of UV-Vis light irradiation. The excellent water solubility and presence of small amount of anatase crystallinity which formed the surface-phase junctions between the rutile and anatase nanoparticles and presence of amorphous carbon is responsible for achieving higher photo-catalytic activity of TCNs.

A relatively higher electrochemical performance and 52 times larger cathodic current density is obtained in TCNs in compared to that in CTP. TCNs exhibit extremely high hydrogen evolution reaction (HER) catalytic activity with very small onset overpotential. The abundant active edge sites in TCNs are responsible for achieving such high HER performance. The present study has opened up a new possibility of fabrication of TCNs, with high photo-catalytic and electrochemical performance, by a low-cost technique and by using only bio-precursor.

Experimental procedures

Synthesis of TCNs nanostructures

The Banana (*Musa balbisiana*) bracts are collected from the local market of Bankura district, West Bengal, India having the market price of ~Rs. 30/kg (~$ 0.5/kg). The collected bracts are gently washed by distilled and deionised water several times to remove dust and the bracts are then cut into small pieces. The bracts are shade dried under the sun light about 3 day under dust free condition. Then the dried product is grinded and sieved to get the finest powder. Typically, 7 g of the dried powder is mixed with 100 ml of methanol and left it undisturbed at room temperature. After 3 day, resulting solution is filtered through Whatman filter paper (Cat no-101090), 40 ml of the solution is transferred to the autoclave. After that the autoclave is sealed and heated at 140°C for 3h and 6h and henceforth the samples synthesized after 3h and 6h will be called as S1 and S2, respectively, unless otherwise specified. After cooling to room temperature naturally, the products are washed repeatedly with methanol and are dried at room temperature for 12 h to obtain powders. In order to find out the change in optical properties and efficiency of photo-catalytic activity under visible light, S2 sample has been annealed at 200°C and 400°C, those are identified as S2#200C and S2#400C.
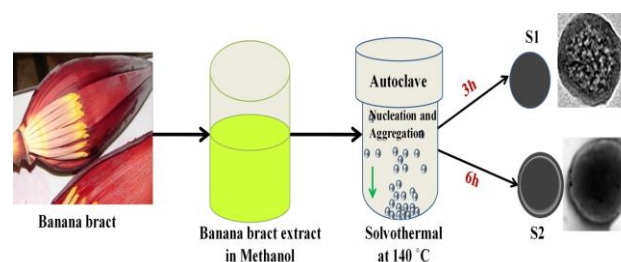

Fig. 1 The schematic illustration for the process of formation of TCNs.

Characterizations

UV-Vis absorption spectra of the synthesized samples dispersed in DI water are recorded in the wavelength range of 200–800 nm with a double beam UV-Vis spectrophotometer (Model: Hitachi U-3010). The PL emission properties of the samples are measured at room temperature using a PL spectrofluorometer (Model: Perkin Elmer LS-55) equipped with a pulsed Xenon discharge lamp as a source of excitation, and an excitation wavelength of 325 nm has been used for all the samples.

UV-Vis absorption and PL emission spectra are measured by dispersing equal amounts of powder samples in 20 ml DI water which is then ultrasonicated for dispersion. The evaluation of phase and structure of the synthesized samples has been carried out by using an X-ray diffractometer (PANLYTICAL) with Cu K$_\alpha$ radiation of wavelength $\lambda = 0.15406$ nm in the scan range of 20–70° (*2θ*). The morphologies and sizes of the samples are determined by dispersing them on carbon coated copper grid and observed in transmission electron microscopy (TEM).

Measurements of photo-catalytic activities

Photo-catalytic activities of as-synthesized S1 and S2 samples, annealed S2#200C and S2#400C samples and CTP have been studied by monitoring the degradation of MB dye in aqueous medium under 125 W UV-Vis and 250 W visible light irradiation. The experiments are carried out in a quartz reactor and 125 W and 250 W Hg lamps (Photo chemical reactor, Lelesil Innovative System) are used as the UV-Vis/Visible light source. The temperature of the reactor is controlled throughout the experiments by circulating water in the jacketed wall reactor. At regular time intervals 5 ml of sample have been collected from the reactor, and after centrifugation UV-Vis absorption spectra have been taken to monitor the degradation of MB dye by monitoring the characteristic absorption peak intensity at ~ 664 nm. In a typical experiment, 50 ml solution of MB dye of concentration 0.02 g/L is loaded with 0.002 g of the synthesized samples or CTP then the solutions are transferred into the photo-chemical reactor. The absorption behavior of MB dye with the synthesized samples is also studied before the UV-Vis/Visible light irradiation. For the adsorption measurements, the MB dye solution loaded with photo-catalyst is stirred continuously in the dark for 40 min and 5 ml solution is collected from the reactor at regular time intervals. The absorbance of the sample is measured after centrifugation at the maximum absorbance wavelength of 664 nm and it is found that after 40 min adsorption equilibrium is established.

Measurements of electrochemical performance

The electrochemical behavior of S1, S2 sample and CTP are investigated in 0.5 M H_2SO_4 aqueous electrolyte solution under a three-electrode cell set-up at room temperature. The electrochemical property of the samples is measured by preparing a film on the Indium tin oxide (ITO). Films have been prepared by drop casting method. Platinum mess is used as the counter electrode and Ag/AgCl as the reference electrode and our as prepared films are as a working electrode. Cyclic voltammetry (CV) studies are carried out by using a computer controlled potentiostate (K-Lyte 1.0) in the potential range of -0.5 to 1.5 V.

Results and discussion

Structural analysis

The XRD patterns of S1 and S2 samples are shown in the **Fig. 2(a)**. The streak patterns of rutile and anatase phase

according to ICSD file number (ICSD card 082081 for rutile and ICSD card 00-021-1272 for anatase) are also plotted in **Fig. 2(a)**, green pattern for rutile while blue for anatase phase of TiO_2.
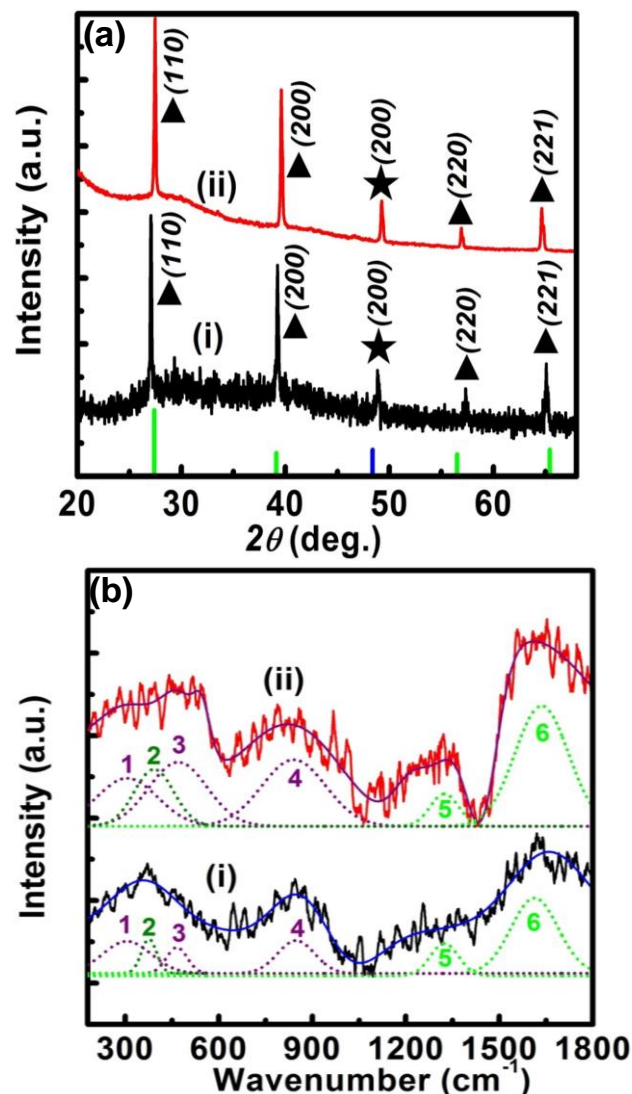

Fig. 2. (a) XRD diffraction pattern of as-synthesized TCNs showing the co-existence of rutile and anatase phases in both S1 (i) and S2 (ii), (b) Raman spectra of S1 (i) and S2 (ii) sample and the corresponding Gaussian fitted curves are shown in different colors and numbered as 1-6. 1, 3, and 4 designate rutile phase, 2 for anatase phase of TiO_2 and 5 & 6 is for amorphous carbon.

The XRD pattern of S1 and S2 (**Fig. 2(a)**) show several weak characteristic peaks which are nearly matched to standard peak position of rutile and anatase phase, demonstrating the very poor crystallinity of the sample, with the majority of the component remaining amorphous. A very strong peak is observed at $2\theta=27.16°$ and $27.46°$ for S1 and S2 sample, respectively, nearly equal to (*110*) plane of rutile phase of TiO_2 nanoparticles. The presence of XRD peaks due to other planes, namely (*200*), (*220*), and (*221*) (ICSD card 082081) have also nearly matched to the rutile phase. One anatase (*200*) peak (ICSD card 00-021-1272) is observed in both of S1 and S2 samples whereas no significant crystalline plane of the carbon is found, suggesting its amorphous nature. Thus, the

presence of anatase and rutile phase of TiO_2 is confirmed by the XRD data analyses. We have estimated the particle size using Debye-Scherer formula given below.

$$D = \frac{0.9\lambda}{\beta \cos\theta} \qquad (1)$$

Inter planer spacing between atoms is calculated from Bragg's Law.

$$2d \sin\theta = n\lambda \qquad (2)$$

where, λ is wavelength of X-Ray (0.15406 nm), β is FWHM (full width at half maximum), θ is diffraction angle, d is the inter planer spacing and D is the particles size. The results obtained from XRD analysis and the particle size of the samples has been estimated to be 45 nm and 60 nm for S1 and S2, respectively. The corresponding interplanar positions are shown in the **Table S1** (supplementary information) which is well matched to standard ICSD files. We have seen from XRD analysis that no such prominent peaks of other materials are observed in our samples. As our synthesis process is related to green source, there is a great chance to exhibit the presence of carbon.
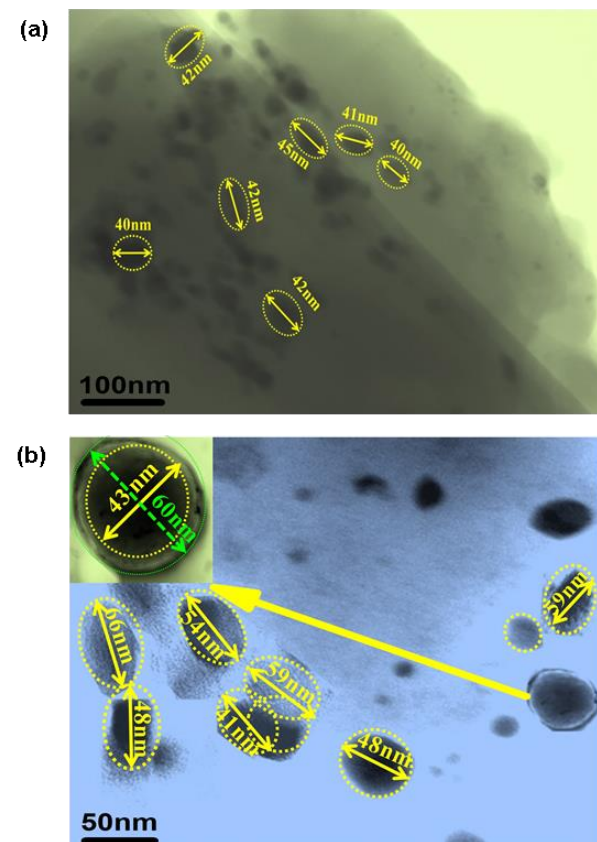
Fig. 3. (a) TEM image showing the morphology of S1. Nearly spherical like nanoparticles are identified by yellow dotted circles. (b) TEM image showing the morphology of S2 (Inset shows a hollow spherical particle with inner diameter of 43 nm and outer diameter of 60 nm). Nearly spherical like nanoparticles are also identified by yellow dotted circles.

Raman spectra are also recorded to find out the structural features of the composite materials and it is shown in **Fig. 2(b)**. The experimental data is fitted with Gaussian fitting and from the fitted curve it is found that Raman spectra of S1 and S2 (**Fig. 2(b)**) exhibit four modes assigned to TiO_2 owing to two phases co-existed. S1 and S2 both possesses a weak peak at 377 cm^{-1} (S1) and 393 cm^{-1} (S2) corresponding to B_{1g} of anatase phase and the bands at 300 (304), 464 (468) and 840 (841) cm^{-1} for S1 (S2) are assigned to E_g and B_{2g} vibrational modes of rutile phase, respectively [1, 17]. The materials exhibiting two broad peaks with intensity maxima close to 1318 cm^{-1} (D band), related to imperfections in the carbon structure. The G band associated to the E_{2g} vibrational mode of sp^2 bonded carbon atoms is observed at ~ 1610 cm^{-1} and ~1630 cm^{-1} in S1 and S2, respectively [18-20]. The appearances of these characteristic peaks demonstrate that amorphous carbon exists in the composite. The intensity of the peaks corresponding to TiO_2 is increased as the solvothermal time of synthesis is increased. As reported earlier that TiO_2 can be produced from ore Ilmenite [11, 12] and Ilmenite is present in the soil of the district of Bankura and Purulia of West Bengal, India (according to database of Directorate of Mines & Minerals, Government of West Bengal-http://www. dmm.gov.in/htmls/mineral-inventory. html) from where we have collected banana bract. This has perhaps led to the formation of TiO_2@C nanocomposite after solvothermal treatment of banana bract extract prepared in methanol medium.

Surface morphological analysis

TEM images of synthesized TCNs are presented in **Figs. 3(a)-3(b)**. Some nearly spherical shape nanoparticles having the sizes ~ 40 nm are clearly identified from **Fig. 3(a)**. Along-with the solid TCNs some hollow shaped TCNs are also evident from TEM image of **Fig. 3(b)**. An enlarged image of hollow TCNs is shown in the inset picture of **Fig. 3(b)**.

Optical properties of TCNs

UV-Vis absorption spectra of the synthesised S1 and S2 samples as well as those of annealed S2#200C and S2#400C samples are shown in **Fig. 4(a)**. It is observed from the **Fig. 4(a)** that all samples exhibit absorption in the UV region and a few shoulder peaks are present in visible region. The absorption peak at ~ 247 nm (S1), 258 nm (S2), 232 nm (S2#200C) and 231 nm (S2#400C) are assigned to be $\pi-\pi^*$ transition of amorphous carbon. Another peak at 300 nm (S1), 299 nm (S2), 280 nm (S2#200C) and 284 nm (S2#400C) is ascribed to n$-\pi^*$ transition [10, 21]. The absorption band around 360 nm is due to phonon assisted indirect transition from edge to the center ($O_{2p}{\rightarrow}Ti_{3d}$) of Brillouin zone of TiO_2 [22]. A visible hump appeared at ~ 420 nm is attributed to oxygen vacancy with two trapped electrons [23]. The absorption peaks in the wavelength range of 451-620 nm have associated to color centers [23]. Therefore, structural defects such as Ti^{3+} and oxygen vacancies are the reason for the extension of the light absorption of defective TiO_2 up to visible region. The rapid increase of absorbance in

the UV region for S2#200C is caused by the excitation of electrons from the valence band to the conduction band of TiO_2. Lin *et al.* [24] have been synthesized C doped TiO_2 catalyst at different calcinations temperature; they found a long-tail absorption in the visible-light region. As we have seen from Raman spectroscopy data that large amorphous carbon is present in our samples, so the existence of carbon in the sample may have led to appearance of long tail in the visible region.

The room temperature PL emission spectra of the as prepared S1, S2, S2#200C, S2#400C samples and CTP, measured at an excitation wavelength 325 nm, have been presented in **Figs. 4(b)-4(d)** and **Figs. S1(a)-S1(b)** (supplementary information). In order to determine the exact positions of PL emission centers, the experimentally obtained PL emission spectra have been fitted with the Gaussian curves. It has been observed that nature of PL emission spectra obtained in the synthesized samples (**Figs. 4(b)-4(c)** and **Figs. S1(a)-S1(b))** are almost similar to that of CTP (**Fig. 4d**). The first emission peak at 362 nm (S1), 374 nm (S2), 372 nm (S2#200C), 368 nm (S2 # 400C) and 382 nm (CTP) can be ascribed to the annihilation of excitons, whereas the remaining humps may be arising from surface states and surface oxygen vacancies [25-28], such as quasi-free recombination at the absorption band edge, the deep-trap band far below the band edge, the shallow-trap state near the absorption band edge, and a combination of these effects [25]. The band edge emission around 427 nm, 461 nm, 490 nm, 543 nm and 578 nm are attributed due to the surface states are originated due to oxygen vacancies. And surface hydroxyl groups localized within the band gap of synthesized $TiO_2@C$ nanostructures helps to trap the excited state electrons and leads to PL emission at longer wavelength region. The entire PL emission mechanism is shown in **Fig. 4(e)**. It is observed that the surface state emission basically consists of two categories of emission. One set occurs as series giving emissions at 427 nm, 490 nm and 578 nm with almost equal energy difference of 0.37eV. This set of emissions is occurred due to de-excitation of electrons from lower vibronic levels in Ti^{4+} 3d states of TiO_2 lattice to the deep trap levels of (OH^-). The other set of emission arises due to de-excitation of trapping electron and holes from lower vibronic levels of oxygen vacancies of TiO_2 to ground state level. **Fig. 4(c)** inset shows digital photographs of the S2#200C solution, indicating that the TCNs are highly water-soluble. The dispersion displays yellowish-green emission under UV (365 nm) light irradiation.

To evaluate the performance of TCNs to be used in light emitting devices, CIE (Commission Intemationale de I'Eclairage 1931) chromaticity coordinates are calculated [29, 30]. The calculated colour coordinates are (0.18, 0.16), (0.19, 0.19), (0.22, 0.27), and (0.19, 0.16) corresponding to S1, S2, S2#200C and S2#400C samples, respectively. Therefore, it can be stated that the characteristics of light emitted from S2#200C is like that of yellowish-green light. PL emission intensity of S2#200C at the yellowish-green region is the highest in compared to that of other samples. The color hue of the light emitted from the synthesized samples is shown in **Fig. 4(f)**. **Fig. 4(f) inset** shows the variations of the PL

emission peak intensity at 575 nm as obtained in all synthesized samples. It is clearly evident that the S2#200C sample shows highest PL emission intensity at yellowish-green region. Zhang *et al*. [29] have been obtained multicolour emission of blue, cyan, magenta and white from the carbon dots.
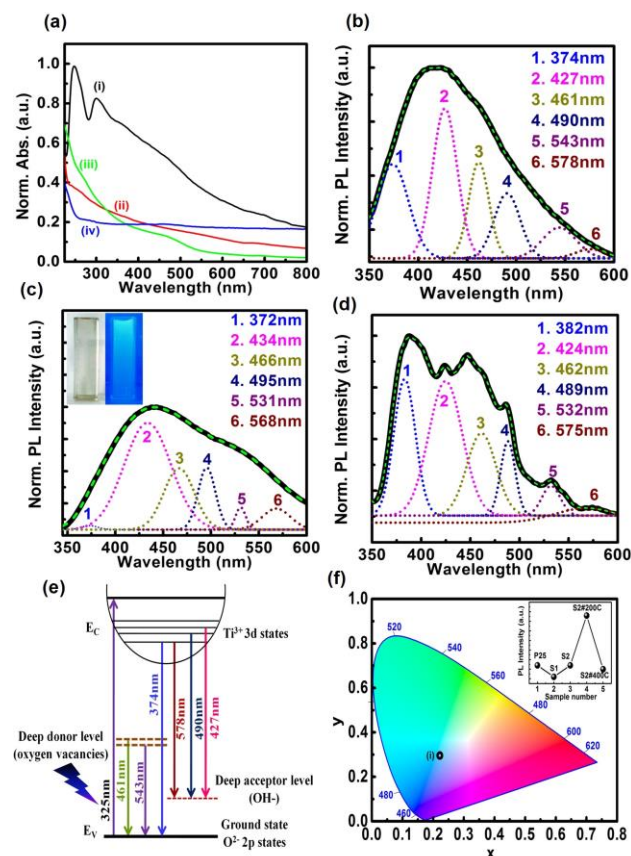

Fig. 4. (a) UV-vis absorption spectra of the synthesized samples, (i) for S1, (ii) for S2, (iii) for S2#200C and (iv) for S2#400C. Room temperature PL emission spectra of S2 (b), S2#200C, (c) (Inset shows the color image when the sample is kept under the UV lamp) and CTP (d), The corresponding Gaussian fitting are also shown in different color corresponding to different peak position and black color line is the experimental curve, (e) Energy band-diagram showing the mechanism of PL emission from TiO_2 nanostructures, (f) CIE chromaticity co-ordinate of sample S2#200 (inset shows the PL emission intensity of the different sample at 575 nm).

Photo-catalytic degradation

We have seen from the UV-Vis absorption spectra that all samples have absorption in the UV region as well as long tails are present in visible region. This has encouraged us to perform photo-catalytic activity under the irradiance of both UV-Vis and visible light. Absorption spectra of MB dye, in the presence of UV-Vis lamp, collected after regular time interval are depicted in **Figs. 5(a)-5(c)** for the sample S1, S2 and CTP, respectively. The S2 sample found to exhibit a higher photo-catalytic activity in comparison with other samples and CTP under UV-Vis light irradiation, which has the highest rate of degradation of over 84% of the organic dye within 100 min. The TCNs can absorb significantly more light in the UV-Vis regions due to transfer of photo-generated electrons from carbon to TiO_2. As a result, the electron-hole pair separation efficiency is increased, which further improve

the activation of TiO_2 for degradation of dye molecules [**31**, **32**]. The digital images as shown in insets of **Figs. 5(a)-5(c)** showed the color of dye solutions. The efficiency of degradation of dye has been calculated and it is found out to be ~71%, ~84% and 68% for S1, S2 and CTP, respectively in 100 min. Here, we have seen that both the synthesized samples give the faster decomposition rate in compared to CTP. It is well established that when the energy of the irradiated light photons is greater than the band gap energy of TCNs, the electrons in the valence band jump to conduction band and create an electron (e^-)-hole (h^+) pair.
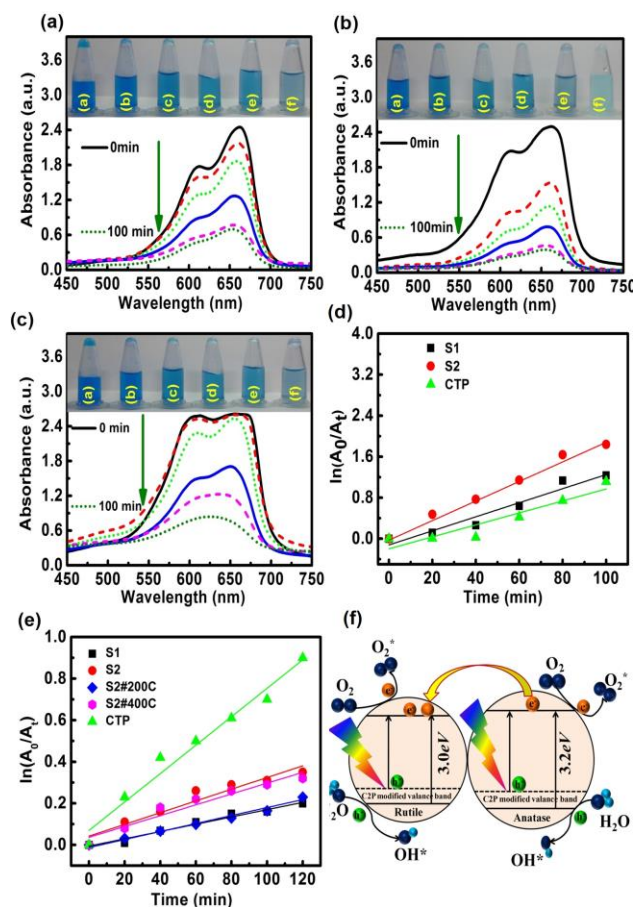
Fig. 5. Methylene blue dye degradation under UV-Vis light irradiation with (a) S1, (b) S2, (c) CTP, (d) First order reaction kinetics of the synthesized samples and that of CTP, (e) First order reaction kinetics of the synthesized samples and that of CTP when visible lights are irradiated, (f) Model of explanation of photo-catalytic properties of the TCNs.

The photo-generated electrons in the conduction band can reduce the dye or react with O2 dissolved in water or adsorbed on the surface of nanoparticles, reducing it to superoxide radical O2•−. The photo-generated holes in the valence band can oxidize the organic molecule to form R+ (oxidation products), or react with H_2O or OH− oxidizing them into OH• radicals.

The relevant reactions at the semiconductor surface causing the degradation of dyes can be expressed as follows [**33**].

$$TCNs + hv \text{ (UV)} \rightarrow TCNs \text{ } (e^-_{CB} + h^+_{VB}) \qquad (3)$$
$$TCNs \text{ } (h^+_{VB}) + H_2O \rightarrow TCNs + H^+ + OH^• \qquad (4)$$

$$TCNs \text{ } (h^+_{VB}) + OH^- \rightarrow TCNs + OH^• \qquad (5)$$
$$TCNs \text{ } (e^-_{CB}) + O_2 \rightarrow TCNs + O_2^{•-} \qquad (6)$$
$$O_2^{•-} + H^+ \rightarrow HO_2^• \qquad (7)$$
$$Dye + OH^• \rightarrow \text{degradation products} \qquad (8)$$
$$Dye + h^+_{VB} \rightarrow \text{oxidation products} \qquad (9)$$
$$Dye + e^-_{CB} \rightarrow \text{reduction products} \qquad (10)$$
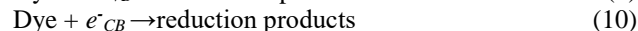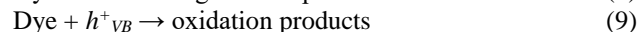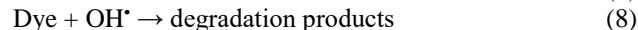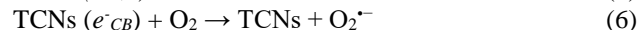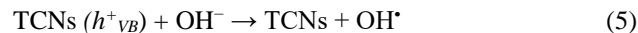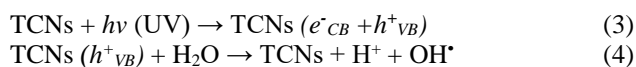
When the chemical concentration A_o is small, the equation of pseudo first-order reaction can be written as [**34**].

$$\ln\left(\frac{A_0}{A_t}\right) = kt \qquad (11)$$

where, A_0 is the initial concentration of MB dye and A_t is concentration of MB dye at any time, k is decomposition rate constant. The experimental dye degradation data have been found to follow the pseudo first order kinetics as given by the equation (11) and the linear fittings are shown in **Fig. 5(d)**. The black squares, red circles and green triangles in **Fig. 5(d)** are the experimental points corresponding to the synthesized samples S1, S2 and CTP, respectively and the black, red and green lines are their respective linear fittings. The slope of the lines in **Fig. 5(d)** is determined by regression analysis and the decomposition rate constants are found to be ~0.014 min^{-1} for S1, ~0.019 min^{-1} for S2 and ~0.012 min^{-1} for CTP. The photo-catalytic activity of TCNs can be improved by extending the light absorption edge to the visible light region and also improving the light harvesting ability. S2 has high surface area, crystalline order and also presence of some hollow nanostructure in it is responsible for higher photo-catalytic activity. It is well observed that S2 sample shows intense (*110*) peak (**Fig. 2(a)**) in XRD analysis which may facilitate the higher photo-catalytic activity over the other samples [**35**].

It is clear from the UV-Vis absorbance spectra of S1, S2 and annealed S2#200C and S2#400C in **Fig. 4(a)** that the optical response of TCNs shifts into the visible-light region. Previously different research groups [**36**, **37**] have done the photocatalytic activity of TiO_2 and carbon TiO_2 nanocomposites under the visible light. They have achieved the highest MB dye degradation over a long time. So, to get improved efficiency we have done the photocatalytic experiment with visible light and it has given better results. **Figs. S2(a)-S2(e)** (supplementary information) shows the degradation of MB dye in aqueous solution under visible light irradiation. The S2 shows the highest photo-catalytic activity among all samples. It is observed from the slope of the lines in **Fig. 5(e)** that S2 sample shows the highest pseudo first order reaction rate constant of 0.0028 min^{-1} among all synthesized samples. The degradation percentage of MB dye of S1, S2, S2#200C S2#400C and CTP under visible light irradiation are 17%, 29%, 26%, 22% and 59%, respectively in 2h. In case of visible ($\lambda > 420$ nm) light induced photo-catalysis experiments, the mechanism is different from that occurred under UV light irradiation. **Fig. 5(f)** displays the possible mechanism of photo-catalysist. C 2p electrons of amorphous carbon form an acceptor impurity energy level just above the valence band maximum of TiO_2. The absorption spectrum of

TCNs extends to the visible light region and helps to reduce electronic transition energy [38]. Etacheri *et al.* [39] have proposed that the photo-excited electrons from the C 2p level of anatase phase are effectively transferred to the conduction band of rutile causing efficient electron-hole separation. Electron in the conduction band can react with O_2 to produce superoxide radicals ($\bullet O_2^-$). On the other hand, the hole in the valence band reacts with H_2O or OH^- adsorbed on the surface to produce hydroxyl radicals ($\bullet OH$). A comparison of the photocatalytic activities of TCNs with some other published results are summarized in **Table 1.**

And it is found that the TCN, synthesized in this work, has comparable and in some case even higher photocatalytic efficiency in the degradation of MB dye.

Electrochemical characteristics

Figs. 6(a)-6(c) depicts CV profile of S1, S2 and CTP, respectively, in different scan rates from 2 to 9 mV/s. Here from the figures, it can be observed that at lower scan rates there is no prominent redox peak for S1 and CTP. As the sweep rate increases, two redox peaks are arising and the intensity of the peaks is also increased gradually. This might be related to the sequential transitions of Ti^{2+} to Ti^+, and Ti. In case of S2 two reduction peaks are observed at 0.02 V and 0.92 V. It is found from the **Figs. 6(a)** and **6(b)** that all CV curves exhibit approximately rectangular-like shape, indicating that the electrical double-layer formation at the electrode/electrolyte interface [45]. The area under the curves represents the total stored charge which may arise from both faradaic and non-faradaic processes [46]. The total stored charge in the TiO_2 films is strongly dependent on the sweep rate. It is clear from the figures that the anodic and cathodic peak currents (I_p) are linearly dependent on scan rates. A linear relation is obtained between peak currents, and the scan rate indicating that the nature of redox process is controlled in diffusion. It is observed that the cathodic current of our S2 sample exhibits extremely high HER catalytic activity with very small onset overpotential whereas CTP shows very weak HER performance with relative higher onset overpotential and weak cathodic current. Beyond the overpotential the cathodic current is increased very fast and goes to more

negative cathodic current. It is clear from **Fig. 6(b)** that S2 sample exhibits a large cathodic current density of -0.57 mA/cm^2 and CTP gives the highest cathodic current density of -10.67 μA/cm^2 at a scan rate 2 mV/s which is 52 times smaller than our synthesized S2 sample. To provide more insight on the HER catalytic activity of TCNs we have now discussed the HER generation in terms of polarization curve [47].
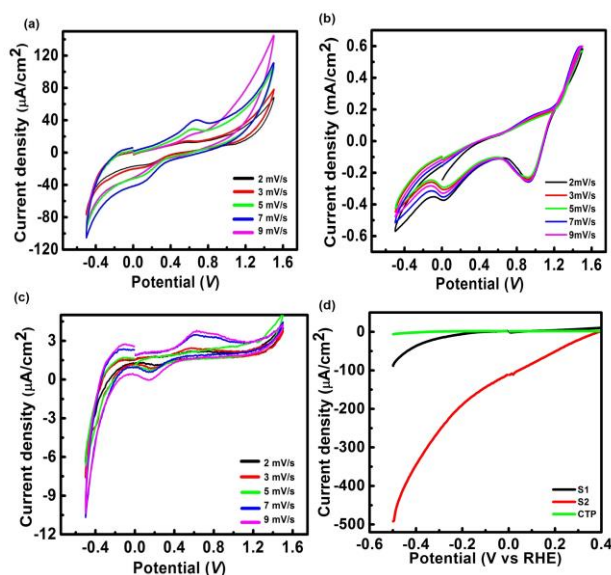

Fig. 6. CV curves of TCNs. (a) for S1, (b) for S2 and (c) for CTP electrodes at different voltage sweep rates from 2 to 9 mV/s, (d) HER performance of S1 (black line), S2(red line), CTP (green line).

The corresponding polarization curves of S1, S2 and CTP at a scan rate of 5 mV/s are shown in the **Fig. 6(d)**. Here we have seen that the S2 sample is giving larger cathodic current with respect to that of CTP. Since the cathodic current density is directly related to the quantity of evolved hydrogen, the large current density here implies prominent hydrogen evolution behavior [47]. The HER activity of TCNs can be increased by increasing the number of active sites on the catalyst, increasing the catalytic activity of the active site and also by improving the electrical contact to these sites. [48] Seebauer *et al.* [49] have mentioned that by defect engineering specific crystal planes may be exposed, and subsequently increase

Table 1. A comparative study of photocatalytic activity of TCNs with previously reported literature.

Synthesis process [Reference]	Irradiated light	Concentration of MB dye (mg/L)	Concentration of catalyst (g/L)	Dye degradation efficiency in % (time in min)
Hydrothermal method [10]	UV	20	C–TiO$_2$ (0.001)	70 (120)
Stirring for 20 h [14]	UV-Vis	6.4	GO–TiO$_2$ (0.33)	<95 (30)
Sacrificial core technique [15]	Solar light	20	sulfur doped hollow TiO$_2$ (0.5)	98.6 (390)
Arc discharge Method [16]	13 Watt fluorescent lamp	20	Mo–TiO$_2$ (3)	89 (120)
Vapour activation [17]	UV	20	TiO$_2$-coated activated carbon (0.5)	~100 (200)
Commercial TiO$_2$ [18]	UV (365nm)	20	P25 (0.1)	74 (60)
Green synthesized TCNs [our result]	UV-Vis (125W)	20	TCNs (0.04)	84 (100)

in the accessible internal surface area is possible. Thus, large number of defects on the basal planes can be expected to increase the exposure of active edge sites by forming cracks on the surfaces of the TCNs **[50]** which may have dramatically improved the electrocatalytic HER performance of TCN. Therefore, developing TCNs electrocatalysts with abundant active edge sites is an efficient way to achieve high HER performance.

Conclusion

In summary, here we have reported the synthesis of TiO$_2$@Carbon nanocomposites from banana bract extract by simple solvothermal process for the first time, to the best of our knowledge, by using green synthesis technique and without using any reducing agent. The synthesized TCNs (S2) consisting of some hollow shaped particles showed the highest dye degradation efficiency of 84% for the degradation of MB dye under the irradiation of UV-Vis light. The obtained value of the degradation efficiency of S2 sample is 16% higher than that of commercially available TiO$_2$ powder (i.e. CTP) The prepared samples showed first order reaction kinetics while the degradation of dye and by linear fitting of the experimental data the highest decomposition rate constant of 0.019 min^{-1} has been obtained for the synthesized sample whereas the rate constant of CTP is 0.012 min^{-1}. The TCNs can absorb significantly more light in the UV-Vis regions due to transportation of photo-generated electrons from carbon to the TiO$_2$, which increase the efficiency of separation between the electrons and holes, hence improve the activation of TiO$_2$ for degradation of dye. TCNs exhibit extremely high HER catalytic activity and a large cathodic current density with very small onset overpotential. Therefore, the present green synthesis technique of synthesizing TCNs may open up a new possibility of synthesizing such good catalytic and yellowish-green luminescent material in the commercial scale.
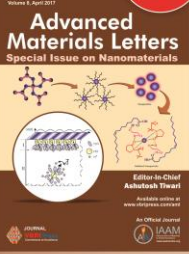
References

1. Zhang, G.; Teng, F.; Wang, Y.; Zhang, P.; Gong, C.; Chen, L.; Zhao, C.; Xie, E.; *RSC Adv.,* **2013**, *3*, 24644.
   DOI: 10.1039/c3ra44950e
2. Zhao, L.; Chen, X.; Wang, X.; Zhang, Y.; Wei, W.; Sun, Y.; Antonietti, M.; Titirici, M. M.; *Adv. Mater.,* **2010**, *22*, 3317.
   DOI: 10.1002/adma.201000660
3. Ashkarrana, A. A.; Fakhari, M.; Hamidinezhad, H.; Haddadi, H.; Nourani, M. R.; *J. Mater. Res. Technol.,* **2015**, *4*, 126.
   DOI: 10.1016/j.jmrt.2014.10.005
4. Ashutosh Tiwari, Y.K. Mishra, H. Kobayashi, A.P.F. Turner (Eds), In the Intelligent Nanomaterials, 2nd Edition, John Wiley & Sons, USA, **2016**.
5. Bozic, M.; Vivod, V.; Vogrincic, R.; Ban, I.; Jaksa, G.; Hribernik, S.; Fakin, D.; Koko, V.; *J. Colloid Interface Sci.,* **2016**, *465*, 93.
   DOI: 10.1016/j.jcis.2015.11.051
6. Irie, H.; Washizuka, S.; Hashimoto, K.; *Thin Solid Films*, **2006**, *510*, 21.
   DOI: 10.1016/j.tsf.2005.08.374
7. Nasrollahzadeh, M.; Sajadi S. M.; *J. Colloid Interface. Sci.,* **2016**, *465*, 121.
   DOI: http://dx.doi.org/10.1016/j.jcis.2015.11.038
8. A.; Shabani, G.; Nabiyouni, J.; Saffari, D.; Ghanbari, *J Mater Sci: Mater Electron*, **2016**, *27*, 8661.
   DOI: 10.1007/s10854-016-4887-5
9. Ashutosh Tiwari, Atul Tiwari (Eds), In the Nanomaterials in Drug Delivery, Imaging, and Tissue Engineering, John Wiley & Sons, USA, **2013**.
10. Wang, J.; Ng, Y. H.; Lim, Y. F.; Ho, G. W.; *RSC Adv.,* **2014**, *4*, 44117.
    DOI: 10.1039/c4ra07290a
11. Tao, T.; Qi-yuan, C.; Hui-ping H.; Zhou-lan, Y.; Ying, C.; *Trans. Nonferrous Met. Soc. China*, **2012**, *22*, 1232.
    DOI: 10.1016/S1003-6326(11)61310-1
12. Foo, K.Y.; Hameed, B.H.; *Adv. Colloid Interface Sci.,* **2010**, *159*, 130.
    DOI: 10.1016/j.cis.2010.06.002
13. Lin, C.; Song, Y.; Cao, L.; Chen, S.; *Nanoscale*, **2013**, *5*, 4986.
    DOI: 10.1039/c3nr01033c
14. Liu, R.; Ren, Y.; Shi, Y.; Zhang, F.; Zhang, L.; Tu, B.; Zhao, D.; *Chem. Mater.*, **2008**, *20*, 1140
    DOI: 10.1021/cm071470w
15. Yu, Y.; Yu, J. C.; Chan, C. Y.; Che, Y. K.; Zhao, J. C.; Ding, L.; Ge, W. K.; Wong, P. K.; *Appl. Catal. B*, **2005**, *61*, 1.
    DOI: http://dx.doi.org/10.1016/j.apcatb.2005.03.008
16. Hurum, D. C.; Agrios, A.. G.; Gray, K. A.; Rajh T.; Thurnauer, M. C.; *J. Phys. Chem. B*, **2003**, *107*, 4545.
    DOI: 10.1021/jp0273934
17. Tripathi, A. K.; Mathpal, M. C.; Kumar, P.; Agrahari, V.; Singh, K. M.; Mishra, K. S.; Ahmad, M. M.; Agarwal, A.; *Adv. Mater. Lett.*, 2015, *6*, 201.
    DOI: 10.5185/amlett.2015.5663
18. Rajan, A.S.; Sampath, S.; Shukla, A. K.; *Energy Environ. Sci.,* **2014**, *7*, 1110.
    DOI: 10.1039/c3ee42783h
19. Wang, L.; Zhang, R.; Jansson, U.; Nedfors, N.; *Sci. Rep.*, **2015**, *5*, 11119.
    DOI: 10.1038/srep11119
20. Wang, H.; Chen, Q. W.; Chen, J. B.; Yu, X.; Hu, X. Y.; *Nanoscale*, **2011**, *3*, 4600.
    DOI: 10.1039/c1nr11012h
21. Songjun Li, Yi Ge, Ashutosh Tiwari, Shunsheng Cao (Eds), In the A Temperature-Responsive Nanoreactor, WILEY-VCH Verlag, USA, **2010**.
22. Mo, S. D.; Chin, W. Y.; *Phys Rev B*, **1995**, *51*, 13023.
    DOI: http://dx.doi.org/10.1103/PhysRevB.51.13023
23. Sekiya, T.; Ichimura, K.; Igarashi, M.; Kurita, S.; *J. Phys. Chem. Solids,* **2000**, *61*, 1237.
    DOI: http://dx.doi.org/10.1016/S0022-3697(99)00424-2
24. Lin, Y. T.; Weng, C. H.; Lin, Y. H.; Shiesh, C. C.; Chen, F. Y.; *Sep. Purif. Technol.,* **2013**, *116*, 114.
    DOI: 10.1016/j.seppur.2013.05.018
25. Mathew, S.; Prasad, A. K.; Benoy, T.; Rakesh, P. P.; Hari, M.; Libish, T. M.; Radhakrishnan, P.; Nampoori, V. P. N.; Vallabhan, C. P. G.; *J. Fluoresc.,* **2012**, *22*, 1563.
    DOI: 10.1007/s10895-012-1096-3
26. Zhao, Y.; Li, C.; Liu, X.; Gu, F.; Jiang, H.; Shao, W.; Zhang, L.; He, Y.; *Mater. Lett*., **2007**, *61*, 79.
    DOI: 10.1016/j.matlet.2006.04.010
27. Atul Tiwari, Ashutosh Tiwari (Eds), Bioengineered Nanomaterials, CRC Press, USA, **2013**.
28. Pan, D.; Zhao, N.; Wang, Q.; Jiang, S.; Ji, X.; An, L.; *Adv. Mater.*, **2005**, *17*, 1991.
    DOI: 10.1002/adma.200500479
29. Zhang, X.; Zhang, Y.; Wang, Y.; Kalytchuk, S.; Kershaw, S. V.; Wang, Y.;Wang, P.; Zhang, T.; Zhao, Y.; Zhang, H.; Cui, T.; Wang, Y.; Zhao, J.; Yu, W. W.; Rogach, A. L.; *ACS Nano,* **2013**, *7*, 11234.
    DOI: 10.1002/anie.201501193
30. Kole, A. K.; Tiwary, C. S.; Kumbhakar, P.; *J. Mater. Chem. C,* **2014**, *2*, 4338.

DOI:10.1039/c4tc00091a

31. Guo, W.; Zhang, F.; Lin, C.; Wang, Z. L.; *Adv. Mater.,* **2012**, *24*, 4761.
   DOI:10.1002/adma.201201075
32. Ashutosh Tiwari, Anthony PF Turner (Eds), Biosensors Nanotechnology, John Wiley & Sons, USA, **2014**.
33. Ma, Y.; Wang, X.; Jia, Y.; Chen, X.; Han, H.; Li, C.; *Chem. Rev.*, **2014**, *114*, 9987.
   DOI:10.1021/cr500008u
34. Lee, C. R.; Kim, H. S.; Jang, I. H.; Im, J. H.; Park, N. G.; *ACS Appl. Mater. Interfaces*, **2011**, *3*, 1953.
   DOI:10.1021/am2001696
35. Du, Y.; Li, J.; Liu, Y.; Niu, X.; Guo, F.; Feng, Q.; *RSC Adv.*, **2016**, *6*, 9717.
   DOI:10.1039/c5ra23451d
36. Shao, X.; Lu, W.; Zhang, R.; Pan, F.; *Sci. Rep.* **2013**, *3*, 3018.
   DOI:10.1038/srep03018
37. Jianga, D.; Xu, Y.; Wu, D.; Sun, Y.; J. *Solid State Chem.,* **2008**, *181*, 593.
   DOI: http://dx.doi.org/10.1016/j.jssc.2008.01.004
38. Shao, P.; Tian, J.; Zhao, Z.; Shi, W.; Gao, S.; Cu, F.; *Appl. Surf. Sci.*, **2015**, *324*, 35.
   DOI:10.1016/j.apsusc.2014.10.108
39. Etacheri, V.; Michlits, G.; Seery, M. K.; Hinder, S. J.; Pillai, S. C.; *ACS Appl. Mater. Interfaces,* **2013**, *5*, 1663.
   DOI:10.1021/am302676a
40. Kim, S. P.; Choi, H. C.; *Bull. Korean Chem. Soc.,* **2014**, *35*, 2660.
   DOI:10.5012/bkcs.2014.35.9.2660
41. Chaudhuri, R. G.; Paria, S.; *Dalton Trans.*, 2014, *43*, 5526.
   DOI:10.1039/c3dt53311e
42. Capek, I. ; Tiwari, A.(Eds), Wiley and Sons, USA, **2015**.
43. Shimizu, N.; Ogino, C.; Dadjour, M. F.; Murata, T.; *Appl. Surf. Sci.,* 2007, *253*, 9254.
   DOI: http://dx.doi.org/10.1016/j.apsusc.2007.05.057
44. Barnes, R. J.; Molina, R.; Xu, J.; Dobson, P. J.; Thompson, I. P.; *J Nanopart. Res*., 2013, *15*, 1432.
   DOI:10.1007/s11051-013-1432-9
45. Vidyadharan, B.; Panikar, A. S.; Ismail, J.; Yusoffa, M. M.; Jose, R.; *RSC Adv.,* **2015**, *5*, 50087.
   DOI:10.1039/c5ra07633a
46. Schopf, D.; Souni, M. E.; *Appl. Phys. A*, **2016**, *122*, 203.
   DOI:10.1007/s00339-016-9730-6
47. Xie , J.; Zhang , H.; Li , S.; Wang , R.; Sun , X.; Zhou , M.; Zhou , J.; Lou , X. W.; Xie, Y.; *Adv. Mater.*, **2013***, 25,* 5807.
   DOI:10.1002/adma.201302685
48. Laursen, A. B.; Kegnaes, S.; Dahla, S.; Chorkendorff, I.; *Energy Environ. Sci.*, **2012**, *5*, 5577.
   DOI:10.1039/c2ee02618j
49. Seebauer, E. G.; Noh, K. W.; *Mater. Sci. Eng. R,* **2010**, *70*, 151.
   DOI: 10.1016/j.mser.2010.06.00
50. Chianelli, R. R.; Ruppert, A. F.; Behai, S. K.; Kear, B. H.; Wold, A.; Kershaw, R.; *J. Catal.*, **1985**, *92*, 56.
   DOI: 10.1016/0021-9517(85)90236-2

Supplementary information

Table S1. Calculation of particle size and lattice parameter from XRD data of TiO₂ nanoparticles.

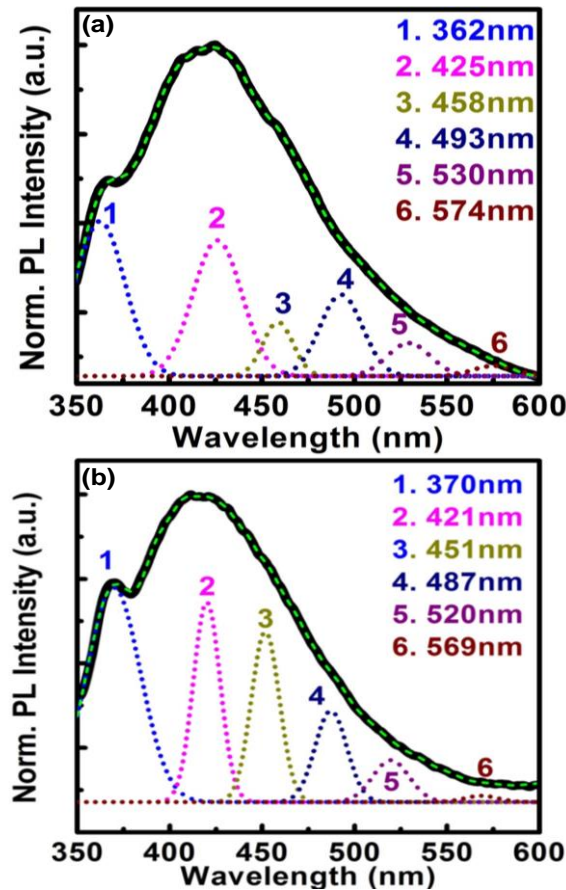| (*hkl*) plane	XRD angle (*2θ in deg.*)		*d* Spacing($\mathring{A}$)	
	S1	**S2**	**S1**	**S2**
(*110*)	27.2	27.46	3.28	3.25
(*200*)	39.32	39.57	2.28	2.27
*(*200*)	48.98	49.32	1.86	1.85
(*220*)	57.40	56.95	1.60	1.62
(*221*)	65.00	64.68	1.43	1.44

Fig. S1. Room temperature PL emission spectra of (a) S1, (b) S2#400C and their Gaussian fitting.
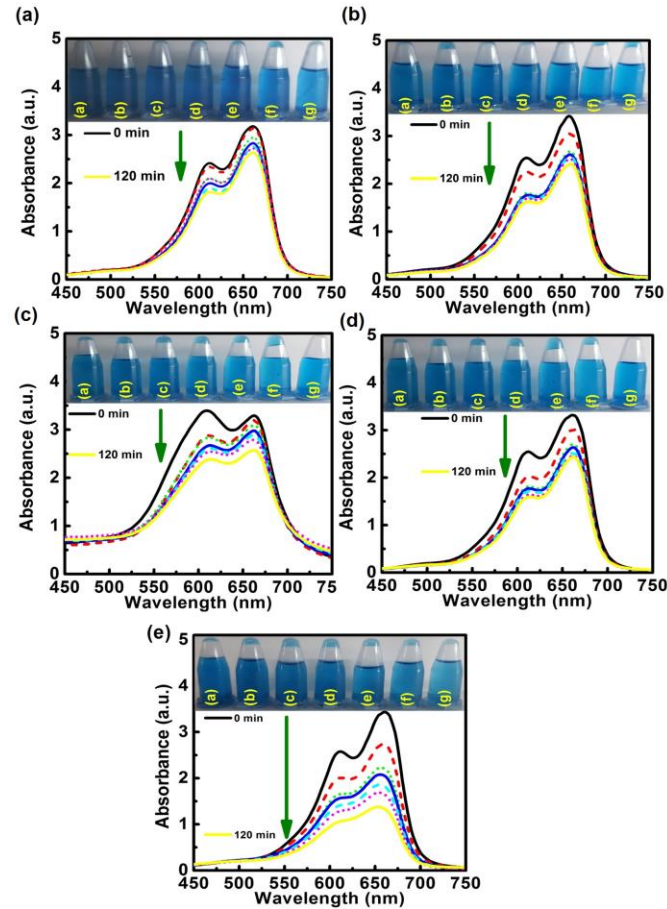

Fig. S2. Methylene blue dye degradation under Visible light (250 *W*) irradiation with (a) S1, (b) S2, (c) S2#200C, (d) S2#400C and (e) CTP.